# Exciton polaritons and hyper-Raman scattering in zinc-blende-type semiconductors: CuBr as an example

B. Hönerlage and U. Rössler
*Institut für Theoretische Physik, Universität Regensburg, D-8400 Regensburg, Bundesrepublik Deutschland*

Vu Duy Phach,* A. Bivas, and J. B. Grun
*Laboratoire de Spectroscopie et d'Optique du Corps Solide, associé au Centre National de la Recherche Scientifique N° 232, Université Louis Pasteur, F-67000 Strasbourg, France*

(Received 17 December 1979)

The dispersion of excitons and hence of excitonic polaritons in zinc-blende-type semiconductors reflects the complexity of the band structure of these materials. We calculate the dispersion of the exciton branches $E_i(\vec{Q})$ of the eightfold ground state from an invariant expansion of the center-of-mass Hamiltonian, including exchange interaction, up to second order in the exciton total wave vector $\vec{Q}$. The excitonic polaritons are then constructed according to Hopfield's polariton theory, which is extended to the case of more than one oscillator. The polariton dispersion is experimentally studied for CuBr by hyper-Raman scattering via biexcitons. The selection rules for this process are calculated for different scattering configurations, whereby the symmetry of the biexciton ground state, having components of $\Gamma_1$, $\Gamma_3$, and $\Gamma_5$ symmetry, is considered. A self-consistent analysis of the observed hyper-Raman emission lines yields the dispersion of the multicomponent excitonic polaritons in CuBr.

## I. INTRODUCTION

The exciton ground state in most direct-gap semiconductors with zinc-blende symmetry is eightfold degenerate at the $\Gamma$ point due to the fourfold degeneracy of the valence-band edge (symmetry $\Gamma_8$) and the twofold degeneracy of the conduction band (symmetry $\Gamma_6$). Exchange interaction splits the eightfold degeneracy into the dipole-allowed $\Gamma_5$ state and the triplet states $\Gamma_3$ and $\Gamma_4$ (Ref. 1). At finite total exciton momentum $\hbar\vec{Q}$ these states may be coupled due to the symmetry-breaking effect of the wave vector. In particular this coupling arises from terms linear[1,2] and quadratic[1,3] in $\vec{Q}$ which derive from corresponding terms in the valence-band Hamiltonian.[4,5] Moreover $\vec{Q}$-dependent exchange terms, which have not been considered so far in the literature, become important in ionic semiconductors, as will be shown in this paper. The effect of all these $\vec{Q}$-dependent terms is to mix exciton states and thus to transfer oscillator strength from the $\Gamma_5$ exciton to some of the triplet-exciton states, which consequently couple with the electromagnetic radiation field. In order to describe this coupling rigorously, we adopt the polariton concept which for the case of a single excitonic oscillator was introduced by Hopfield[6] and Pekar.[7] To account for the more complex exciton structure in zinc-blende compounds this concept has to be extended to the case of different excitonic oscillators. The resulting multicomponent polariton dispersion shows up indirectly in the reflectivity and luminescence spectra.[2,8-10] Direct information on the exciton and/or polariton dispersion may be obtained from nonlinear spectroscopical methods: nonresonant two-photon absorption,[11] resonant Brillouin scattering[12,13] and resonant two-photon Raman (hyper-Raman) scattering.[14-16] These methods are of different applicability, since they allow a study of different parts of the dispersion curves. Two-photon absorption is limited to a study of states with a $\vec{Q}$ vector equal to the sum of the wave vectors of the nonresonant photons, i.e., to states whose wave vector is smaller than that of photons with the same energy. In contrast, resonant Brillouin scattering covers a larger region in reciprocal space, since acoustic phonons are emitted or absorbed. This process is limited, however, by the condition that in the initial and final states the oscillator strength and the coupling to the acoustic phonons are sufficiently large. Resonant two-photon Raman scattering covers a wave vector region up to three times the wave vector of the incident polariton. Moreover, according to the selection rules, exciton states can also be involved which have no oscillator strength.

To outline the last statement we briefly describe the hyper-Raman (HR) scattering process (Fig. 1). Two laser photons (energy $\hbar\omega_l$), which propagate inside the crystal as polaritons with wave vector $\vec{q}_l$ virtually excite a biexciton. The biexciton, serving as an almost resonant intermediate state,[17] decays into two polaritons with energy $E_i(\vec{k})$ and $E_j(\vec{q})$, whereby no relaxation takes place in the intermediate state. Therefore, momentum and energy are conserved in the scattering process:

$$2\vec{q}_l = \vec{q} + \vec{k}, \tag{1}$$

$$2\hbar\omega_l = E_i(\vec{k}) + E_j(\vec{q}). \tag{2}$$

 

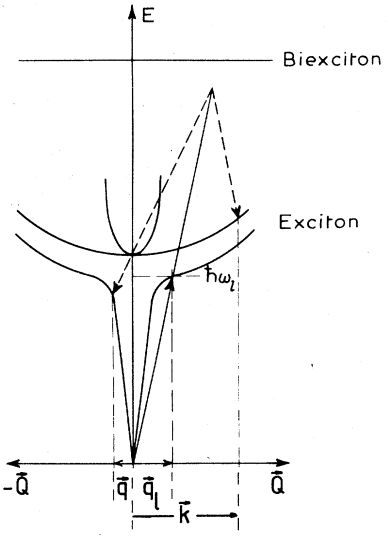


FIG. 1. Schematic picture of the hyper-Raman scattering. The details are discussed in the text.

One of the polaritons, say $E_j(\vec{q})$, is on the lower branch and can be observed as a photon with energy $E_j$ in the emission spectrum, while the second polariton (or exciton) $E_i(\vec{k})$ is not detected. $E_j$ changes its energy if $\hbar\omega_l$ is tuned. Since $\hbar\omega_l$ and $E_j$ are known from the experiment, $E_i$ is determined from Eq. (2). The momentum conservation, however, can be checked only if the dispersion of the exciton and polariton branches $E_i(\vec{k})$, $E_j(\vec{q})$ is known. We use Eqs. (1) and (2) together with the experimental information from hyper-Raman scattering in CuBr to construct directly the dispersion of the exciton and polariton branches, whereby the selection rules for this process—which for this purpose are calculated—are considered. Preliminary results have already been published.[18]

If the biexcitons are generated resonantly, relaxation processes are possible within the biexciton bands. Subsequent decay is a luminescence process, which can be distinguished from the hyper-Raman process since the frequency of the emitted light does not vary with $\omega_l$. Due to the relaxation processes, it is also governed by different selection rules.

The paper is organized as follows. In Sec. II the Hamiltonian for the center-of-mass motion of the eightfold exciton ground state is constructed by group-theoretical methods. Section III is devoted to the construction of biexciton states and to the formulation of selection rules for hyper-Raman scattering. Experimental results for CuBr are given in Sec. IV and analyzed in terms of exciton and polariton dispersion in Sec. V. Concluding remarks are the content of Sec. VI.

## II. THEORY OF MULTICOMPONENT EXCITONS AND POLARITONS

The theory of Wannier excitons in zinc-blende-type semiconductors has to consider the fact, that, due to the valence-band degeneracy, center of mass and relative motion cannot be separated.[19] Calculations of the exciton dispersion have been performed by a variational procedure[20] for different values of the total exciton momentum $\hbar\vec{Q}$, or by a perturbational treatment[3] of the terms which couple relative and center-of-mass motion. Both calculations consider a spinless electron and thus do not take into account the electron-hole exchange interaction.[21] We follow here the more general concept of an invariant expansion[22] of the center-of-mass Hamiltonian whose matrix representation corresponds to expressions given by Cho.[1]

### A. Invariant expansion and exciton matrix

In CuBr, as in most zinc-blende semiconductors, the exciton ground state is eightfold degenerate. A Hamiltonian, acting in this space, can be constructed by means of an invariant expansion[22] from products of the electron-spin operator $\underline{\sigma} = (\sigma_x, \sigma_y, \sigma_z)$ ($\sigma_i$ being Pauli spin matrices) and the hole spin operator $\underline{J} = (J_x, J_y, J_z)$ ($J_i$ being angular momentum matrices for $J = \frac{3}{2}$). Consequently the basis of this eightfold space is given by products of electron states $\alpha$, $\beta$ for spin up and spin down, respectively, and hole states[1]

$$\Phi_1 = -\frac{1}{\sqrt{2}}\begin{pmatrix} x+iy \\ 0 \end{pmatrix}, \quad \Phi_2 = -\frac{1}{\sqrt{6}}\begin{pmatrix} -2z \\ x+iy \end{pmatrix},$$
$$\Phi_3 = \frac{1}{\sqrt{6}}\begin{pmatrix} x-iy \\ 2z \end{pmatrix}, \quad \Phi_4 = \frac{1}{\sqrt{2}}\begin{pmatrix} 0 \\ x-iy \end{pmatrix}, \tag{3}$$

where the [001] direction is used as quantization axis. By Kramer's conjugation of the $\Phi_i$ one obtains the electron states, whose transformation properties are formulated by Koster *et al.*[23] The Hamiltonian obtained reads[1]

$$H^0 = \Delta_0 1_e \otimes 1_h + \Delta_1 \underline{\sigma} \cdot \underline{J} + \Delta_2(\sigma_x J_x^3 + \sigma_y J_y^3 + \sigma_z J_z^3) \tag{4}$$

and describes the splitting of the exciton ground state for zero center-of-mass momentum $\hbar\vec{Q}$ ($1_e$ and $1_h$ are unit matrices of dimension 2 and 4, respectively). This splitting is caused by the isotropic exchange interaction ($\Delta_0, \Delta_1$), and yields the exciton states of symmetry $\Gamma_3 + \Gamma_4$ and $\Gamma_5$ (analytic exchange), which further splits into longitudinal ($\Gamma_{5L}$) and transverse ($\Gamma_{5T}$) states (non-analytic exchange). The anisotropic exchange term ($\Delta_2$) is considered to be small compared to $\Delta_0$ and $\Delta_1$ and is usually neglected.

At finite center-of-mass momentum $\hbar\vec{Q}$ of the

exciton, the Hamiltonian has to be extended by terms containing powers of components of $\vec{Q}$ in the invariant expansion together with those of $\underline{\sigma}$ and $\underline{J}$. These $\vec{Q}$-dependent terms mix the exciton states which at $\vec{Q}=0$ belong to different irreducible representations. The eigenvalues of the $\vec{Q}$-dependent Hamiltonian yield the exciton dispersion.

From the invariant expansion (Appendix) we distinguish two types of $Q$-dependent terms:

(i) The first group is diagonal with respect to the electron states

$$H^1(\vec{Q}) = \Big\{ C_Q[Q_x\{J_x, J_y^2 - J_z^2\} + \text{c.p.}] + G_1 Q^2 1_h + G_2[Q_x^2 (J_x^2 - \tfrac{1}{3} J^2) + \text{c.p.}] + 2G_3[Q_y Q_z \{J_y, J_z\} + \text{c.p.}] \Big\} \otimes 1_e , \tag{5}$$

where $\{A, B\} = (AB+BA)/2$ and c.p. means cyclic permutation. These terms derive directly from corresponding terms of the valence-band effective-mass Hamiltonian,[4,5] in particular $C_Q$ indicates the $\vec{Q}$-linear term, $G_1$ corresponds to the isotropic mass, while $G_2$ and $G_3$ cause splitting and warping of the exciton bands.

(ii) The second group contains the $\vec{Q}$-dependent exchange terms. The invariant expansion up to second order in $\vec{Q}$ yields 11 terms, which are presented in the Appendix. These terms correspond to different orders of perturbation calculation, which is indicated by the power of $\underline{\sigma}$ and $\underline{J}$. Therefore, we consider only those linear in $\underline{\sigma}$ and $\underline{J}$ which can be regarded as the most important ones:

$$H^2(\vec{Q}) = \delta_1 Q^2 \underline{\sigma} \cdot \underline{J} + \delta_2[Q_x^2 (\sigma_x J_x - \tfrac{1}{3} \underline{\sigma} \cdot \underline{J}) + \text{c.p.}] + 2\delta_3[Q_x Q_y \tfrac{1}{2}(\sigma_x J_y + \sigma_y J_x) + \text{c.p.}] . \tag{6}$$

Using the matrix representation for the angular-momentum operators and the Pauli-spin matrices one easily obtains the matrix representation of the total exciton Hamiltonian

$$H = H^0 + H^1(\vec{Q}) + H^2(\vec{Q}) . \tag{7}$$

We transform this matrix from the electron-hole representation to symmetrized exciton wave functions (Table I) which are the same as given by Cho.[1] The resulting matrix is presented in Table II, where we have set $\Delta_2 = 0$ and introduced the splitting $\Delta_{ST}$ between the $\Gamma_3 + \Gamma_4$ and $\Gamma_{5T}$ state and the longitudinal-transverse splitting $\Delta_{LT}$.

It should be mentioned that the parameters of the exciton Hamiltonian Eq. (7) include also polaron corrections, when being used to describe a polar material. The electron-phonon interaction does not contribute separate terms to the invariant expansion.

TABLE I. Symmetrized exciton wave functions according to Ref. 1.

| Symmetry | State | Electron-hole representation |
|---|---|---|
| $\Gamma_3$ | $\|2+\rangle$ | $\frac{1}{\sqrt{2}}(\alpha\Phi_4 - \beta\Phi_1)$ |
| | $\|20\rangle$ | $\frac{1}{\sqrt{2}}(\alpha\Phi_2 - \beta\Phi_3)$ |
| $\Gamma_4$ | $\|1+\rangle$ | $\frac{1}{\sqrt{8}}(\alpha\Phi_1 + \sqrt{3}\alpha\Phi_3 - \sqrt{3}\beta\Phi_2 - \beta\Phi_4)$ |
| | $\|1-\rangle$ | $-\frac{i}{\sqrt{8}}(\alpha\Phi_1 - \sqrt{3}\alpha\Phi_3 - \sqrt{3}\beta\Phi_2 + \beta\Phi_4)$ |
| | $\|2-\rangle$ | $\frac{1}{\sqrt{2}}(\alpha\Phi_4 + \beta\Phi_1)$ |
| $\Gamma_5$ | $\|x\rangle$ | $-\frac{1}{\sqrt{8}}(\sqrt{3}\alpha\Phi_1 - \alpha\Phi_3 + \beta\Phi_2 - \sqrt{3}\beta\Phi_4)$ |
| | $\|y\rangle$ | $-\frac{i}{\sqrt{8}}(\sqrt{3}\alpha\Phi_1 + \alpha\Phi_3 + \beta\Phi_2 + \sqrt{3}\beta\Phi_4)$ |
| | $\|z\rangle$ | $\frac{1}{\sqrt{2}}(\alpha\Phi_2 + \beta\Phi_3)$ |

### B. Results for high-symmetry directions

While for a general direction of the exciton wave vector $\vec{Q}$ the exciton matrix (Table II) can be diagonalized only numerically, it can be represented in block-diagonal form for directions of high symmetry. This form is obtained using exciton wave functions which transform as basis functions of the irreducible representations of the group of $\vec{Q}$.

$\vec{Q} \| [001]$. By specializing the wave vector to $\vec{Q} = (0, 0, Q)$ the matrix (Table II) falls into four blocks, which correspond to the four irreducible representations ($\Delta_i, i = 1, \ldots, 4$) of the point group $C_{2v}$ (Table III), when the following basis transformation is performed:

$$|\zeta \pm\rangle = (1/\sqrt{2})(|x\rangle \pm |y\rangle), \quad |\eta \pm\rangle = (1/\sqrt{2})(|1+\rangle \pm |1-\rangle) . \tag{8}$$

In this case, the eigenvalues and correspondingly the exciton dispersion may be obtained analytically.

$\vec{Q} \| [110]$. We apply the transformation of the exciton functions as given in Table IV, which is equivalent to choosing the [110] crystal direction ($z'$ axis) as the new quantization axis. The matrix representation of the Hamiltonian then falls into blocks corresponding to the two irreducible representations ($\Sigma_1, \Sigma_2$) of the point group $C_s$ (Table V). At $Q=0$, the exciton state $|z\rangle'$ corresponds to the longitudinal exciton ($\Gamma_{5L}$), $|x\rangle'$ and $|y\rangle'$ to the transverse exciton states ($\Gamma_{5T}$). Due to the low symmetry of $\vec{Q}$, longitudinal and transverse states

TABLE II. Matrix representation[a] of the exciton Hamiltonian $H$ [Eq. (7)] in the basis of Table I. Complex conjugated terms of the upper (lower) part have to be added to the lower (upper) part. $\cos\alpha$, $\cos\beta$, $\cos\gamma$ are the direction cosines of $\vec{Q}$ with respect to the [001] direction; $\Delta_{st}$ denotes the splitting between the $\Gamma_3+\Gamma_4$ and $\Gamma_{5T}$ states, $\Delta_{LT}$ the longitudinal-transverse splitting.

| | $\|2+\rangle$ | $\|20\rangle$ | $\|1+\rangle$ | $\|1-\rangle$ |
|---|---|---|---|---|
| $\langle 2+\|$ | $(G_1+\frac{3}{2}\delta_1)Q^2$ $+(G_2+\delta_2)[Q_z^2-\frac{1}{2}(Q_x^2+Q_y^2)]$ | $(\sqrt{3}/2)(G_2+\delta_2)(Q_x^2-Q_y^2)$ | $i\frac{3}{2}(G_3+\delta_3)Q_yQ_z$ | $-i\frac{3}{2}(G_3+\delta_3)Q_xQ_z$ |
| $\langle 20\|$ | | $(G_1+\frac{3}{2}\delta_1)Q^2$ $-(G_2+\delta_2)[Q_z^2-\frac{1}{2}(Q_x^2+Q_y^2)]$ | $-i(\sqrt{3}/2)(G_3+\delta_3)Q_yQ_z$ | $-i(\sqrt{3}/2)(G_3+\delta_3)Q_xQ_z$ |
| $\langle 1+\|$ | $\frac{3}{4}C_QQ_x$ | $-(\sqrt{3}/4)C_QQ_x$ | $(G_1+\frac{3}{2}\delta_1)Q^2$ $+(G_2+\delta_2)[Q_x^2-\frac{1}{2}(Q_y^2+Q_z^2)]$ | $-\frac{3}{2}(G_3+\delta_3)Q_xQ_y$ |
| $\langle 1-\|$ | $-\frac{3}{4}C_QQ_y$ | $-(\sqrt{3}/4)C_QQ_y$ | | $(G_1+\frac{3}{2}\delta_1)Q^2$ $+(G_2+\delta_2)[Q_y^2-\frac{1}{2}(Q_z^2+Q_x^2)]$ |
| $\langle 2-\|$ | | $(\sqrt{3}/2)C_QQ_z$ | | |
| $\langle x\|$ | $-(\sqrt{3}/4)C_QQ_x$ | $-\frac{3}{4}C_QQ_x$ | | $i(\sqrt{3}/2)C_QQ_z$ |
| $\langle y\|$ | $-(\sqrt{3}/4)C_QQ_y$ | $\frac{3}{4}C_QQ_y$ | $-i(\sqrt{3}/2)C_QQ_z$ | |
| $\langle z\|$ | $(\sqrt{3}/2)C_QQ_z$ | | $i(\sqrt{3}/2)C_QQ_y$ | $-i(\sqrt{3}/2)C_QQ_x$ |

| $\|2-\rangle$ | $\|x\rangle$ | $\|y\rangle$ | $\|z\rangle$ |
|---|---|---|---|
| | $i(\sqrt{3}/2)(G_3-\delta_3)Q_yQ_z$ | $i(\sqrt{3}/2)(G_3-\delta_3)Q_xQ_z$ | $-i\sqrt{3}(G_3-\delta_3)Q_xQ_y$ |
| $i\sqrt{3}(G_3+\delta_3)Q_xQ_y$ | $i\frac{3}{2}(G_3-\delta_3)Q_yQ_z$ | $-i\frac{3}{2}(G_3-\delta_3)Q_xQ_z$ | |
| $-\frac{3}{2}(G_3+\delta_3)Q_xQ_z$ | $(\sqrt{3}/2)(G_2-\delta_2)(Q_y^2-Q_z^2)$ | $-(\sqrt{3}/2)(G_3-\delta_3)Q_xQ_y$ | $(\sqrt{3}/2)(G_3-\delta_3)Q_xQ_z$ |
| $-\frac{3}{2}(G_3+\delta_3)Q_yQ_z$ | $(\sqrt{3}/2)(G_3-\delta_3)Q_xQ_y$ | $(\sqrt{3}/2)(G_2-\delta_2)(Q_z^2-Q_x^2)$ | $-(\sqrt{3}/2)(G_3-\delta_3)Q_yQ_z$ |
| $(G_1+\frac{3}{2}\delta_1)Q^2$ $+(G_2+\delta_2)[Q_z^2-\frac{1}{2}(Q_x^2+Q_y^2)]$ | $-(\sqrt{3}/2)(G_3-\delta_3)Q_xQ_z$ | $(\sqrt{3}/2)(G_3-\delta_3)Q_yQ_z$ | $(\sqrt{3}/2)(G_2-\delta_2)(Q_x^2-Q_y^2)$ |
| $-i(\sqrt{3}/2)C_QQ_y$ | $\Delta_{st}+\Delta_{LT}\cos^2\alpha+(G_1-\frac{5}{2}\delta_1)Q^2$ $-(G_2-\frac{1}{3}\delta_2)[Q_x^2-\frac{1}{2}(Q_y^2+Q_z^2)]$ | $-\frac{3}{2}(G_3-\frac{1}{3}\delta_3)Q_xQ_y$ | $-\frac{3}{2}(G_3-\frac{1}{3}\delta_3)Q_xQ_z$ |
| $i(\sqrt{3}/2)C_QQ_x$ | $\Delta_{LT}\cos\alpha\cos\beta$ | $\Delta_{st}+\Delta_{LT}\cos^2\beta+(G_1-\frac{5}{2}\delta_1)Q^2$ $-(G_2-\frac{1}{3}\delta_2)[Q_y^2-\frac{1}{2}(Q_z^2+Q_x^2)]$ | $-\frac{3}{2}(G_3-\frac{1}{3}\delta_3)Q_yQ_z$ |
| | $\Delta_{LT}\cos\alpha\cos\gamma$ | $\Delta_{LT}\cos\beta\cos\gamma$ | $\Delta_{st}+\Delta_{LT}\cos^2\gamma+(G_1-\frac{5}{2}\delta_1)Q^2$ $-(G_2-\frac{1}{3}\delta_2)[Q_z^2-\frac{1}{2}(Q_x^2+Q_y^2)]$ |

[a]Table VIII of Ref. 1 is identical with corresponding terms of our representation if in the matrix elements $\langle 1+\|\,\|x\rangle$, $\langle 1-\|\,\|y\rangle$, and $\langle 2-\|\,\|z\rangle$ the sign of $U_1$ is changed.

TABLE III. Diagonal blocks of the exciton Hamiltonian for $\vec{Q}=(0,0,Q)$.

| $\Delta_1$ | $\|2+\rangle$ | $\|z\rangle$ |
|---|---|---|
| $\langle 2+\|$ | $(G_1+\frac{3}{2}\delta_1+G_2+\delta_2)Q^2$ | $(\sqrt{3}/2)C_Q Q$ |
| $\langle z\|$ | $(\sqrt{3}/2)C_Q Q$ | $\Delta_{St}+\Delta_{LT}+(G_1-\frac{5}{2}\delta_1-G_2+\frac{1}{3}\delta_2)Q^2$ |
| $\Delta_2$ | $\|20\rangle$ | $\|2-\rangle$ |
| $\langle 20\|$ | $(G_1+\frac{3}{2}\delta_1-G_2-\delta_2)Q^2$ | $(\sqrt{3}/2)C_Q Q$ |
| $\langle 2-\|$ | $(\sqrt{3}/2)C_Q Q$ | $(G_1+\frac{3}{2}\delta_1+G_2+\delta_2)Q^2$ |
| $\Delta_3$ | $\|\eta-\rangle$ | $\|\xi+\rangle$ |
| $\langle\eta-\|$ | $(G_1+\frac{3}{2}\delta_1-\frac{1}{2}G_2-\frac{1}{2}\delta_2)Q^2$ | $i(\sqrt{3}/2)C_Q Q-(\sqrt{3}/2)(G_2-\delta_2)Q^2$ |
| $\langle\xi+\|$ | $-i(\sqrt{3}/2)C_Q Q-(\sqrt{3}/2)(G_2-\delta_2)Q^2$ | $\Delta_{St}+(G_1-\frac{5}{2}\delta_1+\frac{1}{2}G_2-\frac{1}{6}\delta_2)Q^2$ |
| $\Delta_4$ | $\|\eta+\rangle$ | $\|\xi-\rangle$ |
| $\langle\eta+\|$ | $(G_1+\frac{3}{2}\delta_1-\frac{1}{2}G-\frac{1}{2}\delta_2)Q^2$ | $-i(\sqrt{3}/2)C_Q Q-(\sqrt{3}/2)(G_2-\delta_2)Q^2$ |
| $\langle\xi-\|$ | $i(\sqrt{3}/2)C_Q Q-(\sqrt{3}/2)(G_2-\delta_2)Q^2$ | $\Delta_{St}+(G_1-\frac{5}{2}\delta_1+\frac{1}{2}G_2-\frac{1}{6}\delta_2)Q^2$ |

are mixed in the representation $\Sigma_1$.

$\vec{Q}\parallel[111]$. Choosing the [111] direction as new quantization axis ($\vec{z}'\parallel[111]$), we obtain the symmetrized exciton basis of Table IV. The resulting diagonal blocks of the Hamiltonian are given in Table VI. The blocks correspond to the irreducible representations $\Lambda_1$, $\Lambda_2$, and $\Lambda_3$ of the point group $C_{3v}$. As is seen from Table VI, the twofold representation $\Lambda_3$ contains the transverse exciton states $|x\rangle'$ and $|y\rangle'$. For $Q\neq 0$, the $3\times 3$ matrices have to be diagonalized numerically.

It is interesting to point out that, for vanishing $\vec{Q}$-linear interactions and vanishing exchange terms, the block matrices given in Tables III, V, and VI can be diagonalized for all $\vec{Q}$ values analytically, giving in each direction rise to two different eigenvalues which are fourfold degenerate. The dispersion thus obtained corresponds to the "light" and "heavy" excitons.[3,24] In this approximation the effective masses of the light and heavy excitons can be related to the Luttinger parameters $\gamma_1$, $\gamma_2$, and $\gamma_3$ and to the electron effective mass $m_e$. By comparison with the results of Kane,[3] we find

$$\begin{aligned} G_1&=\hbar^2/2M_a\,,\\ G_2&=(\hbar^2\beta_\hbar^2/m_0)\gamma_2\,,\\ G_3&=(\hbar^2\beta_\hbar^2/m_0)\gamma_3\,, \end{aligned} \tag{9}$$

where $m_0$ is the free electron mass. $M_a$ is a function which is tabulated in Ref. 3, and $\beta_\hbar=(m_0/m_e)/(\gamma_1+m_0/m_e)$. Inclusion of $\vec{Q}$-linear and exchange interactions changes the exciton dispersion considerably, however.

TABLE IV. Exciton wave functions for $\vec{Q}$ along the high-symmetry directions [110] and [111] which are taken as quantization axis.

| New basis | Linear combination of basis functions from Table I: $\vec{Q}\parallel[110]$ | $\vec{Q}\parallel[111]$ |
|---|---|---|
| $\|2+\rangle'$ | $\frac{1}{2}(-\sqrt{3}\|20\rangle+i\|2-\rangle)$ | $\|2+\rangle$ |
| $\|20\rangle'$ | $-\frac{1}{2}(\|20\rangle+i\sqrt{3}\|2-\rangle)$ | $\|20\rangle$ |
| $\|1+\rangle'$ | $(1/\sqrt{2})(\|1+\rangle+\|1-\rangle)$ | $(1/\sqrt{2})(\|1+\rangle-\|1-\rangle)$ |
| $\|1-\rangle'$ | $-i\|2+\rangle$ | $(1/\sqrt{6})(2\|2-\rangle-\|1+\rangle-\|1-\rangle)$ |
| $\|2-\rangle'$ | $(1/\sqrt{2})(\|1+\rangle-\|1-\rangle)$ | $(1/\sqrt{3})(\|1+\rangle+\|1-\rangle+\|2-\rangle)$ |
| $\|x\rangle'$ | $(1/\sqrt{2})(-\|x\rangle+\|y\rangle)$ | $(1/\sqrt{2})(-\|x\rangle+\|y\rangle)$ |
| $\|y\rangle'$ | $\|z\rangle$ | $(1/\sqrt{6})(2\|z\rangle-\|x\rangle-\|y\rangle)$ |
| $\|z\rangle'$ | $(1/\sqrt{2})(\|x\rangle+\|y\rangle)$ | $(1/\sqrt{3})(\|x\rangle+\|y\rangle+\|z\rangle)$ |

TABLE V. Diagonal blocks of the exciton Hamiltonian for $\vec{Q}=(1/\sqrt{2})(Q,Q,0)$. Complex conjugate terms of the lower (upper) part have to be added to the upper (lower) part.

| $\Sigma_1$ | $\lvert 1-\rangle'$ | $\lvert 2-\rangle'$ | $\lvert y\rangle'$ | $\lvert z\rangle'$ |
|---|---|---|---|---|
| $\langle 1-\rvert'$ | $(G_1+\frac{3}{2}\delta_1-\frac{1}{2}G_2-\frac{1}{2}\delta_2)Q^2$ | | $(\sqrt{3}/2)(G_3-\delta_3)Q^2$ | |
| $\langle 2-\rvert'$ | $-i\frac{3}{4}C_Q Q$ | $(G_1+\frac{3}{2}\delta_1+\frac{1}{4}G_2+\frac{1}{4}\delta_2+\frac{3}{4}G_3+\frac{3}{4}\delta_3)Q^2$ | | $(\sqrt{3}/4)(G_2-\delta_2-G_3+\delta_3)Q^2$ |
| $\langle y\rvert'$ | | $i(\sqrt{3}/2)C_Q Q$ | $\Delta_{St}+(G_1-\frac{5}{2}\delta_1+\frac{1}{2}G_2-\frac{1}{6}\delta_2)Q^2$ | 0 |
| $\langle z\rvert'$ | $i(\sqrt{3}/4)C_Q Q$ | | 0 | $\Delta_{St}+\Delta_{LT}+(G_1-\frac{5}{2}\delta_1-\frac{1}{4}G_2+\frac{1}{12}\delta_2-\frac{3}{4}G_3+\frac{1}{4}\delta_3)Q^2$ |
| $\Sigma_2$ | $\lvert 2+\rangle'$ | $\lvert 20\rangle'$ | $\lvert 1+\rangle'$ | $\lvert x\rangle'$ |
| $\langle 2+\rvert'$ | $(G_1+\frac{3}{2}\delta_1+\frac{1}{4}G_2+\frac{1}{4}\delta_2+\frac{3}{4}G_3+\frac{3}{4}\delta_3)Q^2$ | $(\sqrt{3}/4)(G_2+\delta_2-G_3-\delta_3)Q^2$ | | |
| $\langle 20\rvert'$ | | $(G_1+\frac{3}{2}\delta_1-\frac{1}{4}G_2-\frac{1}{4}\delta_2-\frac{3}{4}G_3-\frac{3}{4}\delta_3)Q^2$ | | |
| $\langle 1+\rvert'$ | $\frac{3}{8}C_Q Q$ | $(\sqrt{3}/8)C_Q Q$ | $(G_1+\frac{3}{2}\delta_1+\frac{1}{4}G_2+\frac{1}{4}\delta_2-\frac{3}{4}G_3-\frac{3}{4}\delta_3)Q^2$ | $-(\sqrt{3}/4)(G_2-\delta_2+G_3-\delta_3)Q^2$ |
| $\langle x\rvert'$ | $-(5\sqrt{3}/8)C_Q Q$ | $\frac{3}{8}C_Q Q$ | | $\Delta_{St}+(G_1-\frac{5}{2}\delta_1-\frac{1}{4}G_2+\frac{1}{12}\delta_2+\frac{3}{4}G_3-\frac{1}{4}\delta_3)Q^2$ |

### C. Multicomponent excitonic polaritons

As discussed above, the Schrödinger equation for the exciton system

$$H\lvert\psi_i(\vec{Q})\rangle = E_x^n(\vec{Q})\lvert\psi_i(\vec{Q})\rangle \tag{10}$$

may be solved numerically. The result gives the exciton dispersion $E_x^n(\vec{Q})$ and the eigenvectors in the form

$$\lvert\psi_i(\vec{Q})\rangle = \sum_j C_{ij}(\vec{Q})\lvert\psi_j\rangle\,, \tag{11}$$

TABLE VI. Diagonal blocks of the exciton Hamiltonian for $\vec{Q}=(1/\sqrt{3})(Q,Q,Q)$. Complex conjugate terms of the lower (upper) part have to be added to the upper (lower) part.

| $\Lambda_1$ | $\lvert z\rangle'$ |
|---|---|
| $\langle z\rvert'$ | $\Delta_{st}+\Delta_{LT}+(G_1-\frac{5}{2}\delta_1-G_3+\frac{1}{3}\delta_3)Q^2$ |
| $\Lambda_2$ | $\lvert 2-\rangle'$ |
| $\langle 2-\rvert'$ | $(G_1+\frac{3}{2}\delta_1-G_3-\delta_3)Q^2$ |

| $\Lambda_3$ (1st row) | $\lvert 2+\rangle'$ | $\lvert 1+\rangle'$ | $\lvert y\rangle'$ |
|---|---|---|---|
| $\langle 2+\rvert'$ | $(G_1+\frac{3}{2}\delta_1)Q^2$ | $(i/\sqrt{2})(G_3+\delta_3)Q^2$ | $-(i/\sqrt{2})(G_3-\delta_3)Q^2$ |
| $\langle 1+\rvert'$ | $(\sqrt{3}/2\sqrt{2})C_Q Q$ | $(G_1+\frac{3}{2}\delta_1+\frac{1}{2}G_3+\frac{1}{2}\delta_3)Q^2$ | $\frac{1}{2}(G_3-\delta_3)Q^2$ |
| $\langle y\rvert'$ | $(\sqrt{3}/2\sqrt{2})C_Q Q$ | $(i\sqrt{3}/2)C_Q Q$ | $\Delta_{st}+(G_1-\frac{5}{2}\delta_1+\frac{1}{2}G_3-\frac{1}{6}\delta_3)Q^2$ |

| $\Lambda_3$ (2nd row) | $\lvert 20\rangle'$ | $\lvert 1-\rangle'$ | $\lvert x\rangle'$ |
|---|---|---|---|
| $\langle 20\rvert'$ | $(G_1+\frac{3}{2}\delta_1)Q^2$ | $(i/\sqrt{2})(G_3+\delta_3)Q^2$ | $-(i/\sqrt{2})(G_3-\delta_3)Q^2$ |
| $\langle 1-\rvert'$ | $(\sqrt{3}/2\sqrt{2})C_Q Q$ | $(G_1+\frac{3}{2}\delta_1+\frac{1}{2}G_3+\frac{1}{2}\delta_3)Q^2$ | $+\frac{1}{2}(G_3-\delta_3)Q^2$ |
| $\langle x\rvert'$ | $+(\sqrt{3}/2\sqrt{2})C_Q Q$ | $+i(\sqrt{3}/2)C_Q Q$ | $\Delta_{st}+(G_1-\frac{5}{2}\delta_1+\frac{1}{2}G_3-\frac{1}{6}\delta_3)Q^2$ |

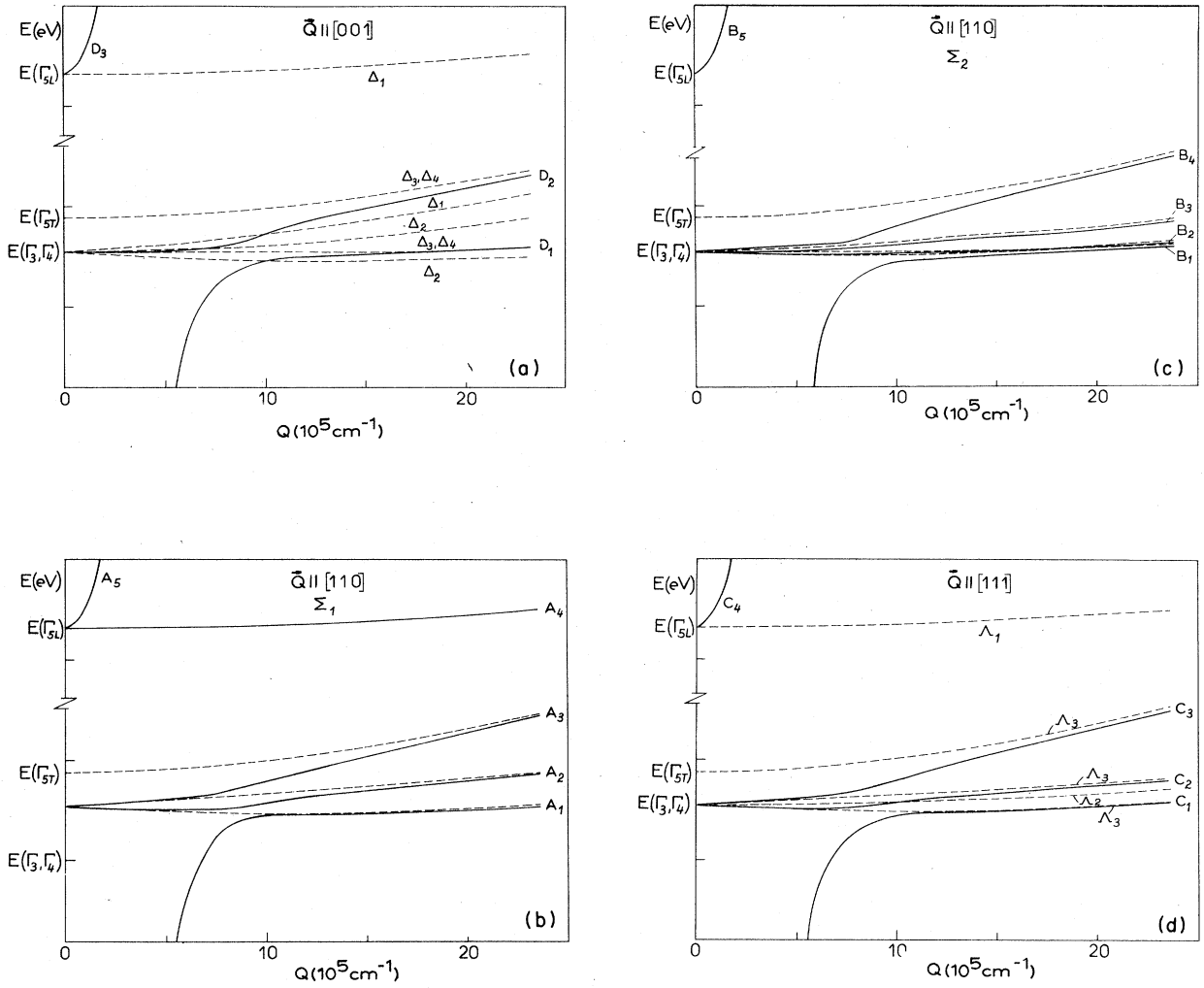


FIG. 2. Dispersion of excitons (dashed lines) and of excitonic polaritons (full lines) in zinc-blende-type materials for different directions of the wave vector $\vec{Q}$. (a) $\vec{Q}\parallel[001]$, $\Delta_i (i=1,\ldots,4)$ indicate the irreducible representations of the different branches. (b) $\vec{Q}\parallel[110]$, all branches have $\Sigma_1$ symmetry. (c) $\vec{Q}\parallel[110]$, all branches have $\Sigma_2$ symmetry. (d) $\vec{Q}\parallel[111]$, $\Lambda_i (i=1,2,3)$ indicate the irreducible representations of the different branches.

where $|\psi_j\rangle$ are the symmetrized exciton wave functions of Table I. The transverse exciton states (denoted $\Gamma_{5T}$ at $\vec{Q}=0$) couple strongly to the electromagnetic radiation field, while the triplet states with $\Gamma_3$ and $\Gamma_4$ symmetry do not couple. Due to the $\vec{Q}$-dependent interaction at finite $\vec{Q}$ there may be an admixture of the transverse exciton states also to the triplet and longitudinal states. The eigenstates of the coupled dipole-active exciton-photon system have been shown to be polaritons.[6,7] Due to the more complicated exciton structure in the present case, the simple one-oscillator model[6,7] has to be extended to the multiple oscillator case.[2] The solution $E_{j\rho}(\vec{Q}) = \hbar\omega$ of the equation

$$n^2(\vec{Q},\omega) = \frac{Q^2c^2}{\omega^2} = \epsilon_b + \sum_{\mu} \frac{\epsilon_b C_{5\mu}^2(\vec{Q})[E^2(\Gamma_{5L}) - E^2(\Gamma_{5T})]}{E_x^{\mu}(\vec{Q})^2 - \hbar^2\omega^2} \tag{12}$$

defines the polariton dispersion $E_{j\rho}(\vec{Q})$. The index $j$ labels the polariton branch and $\rho$ the irreducible representation under consideration, if one studies one of the high-symmetry directions. The refractive index is given by $n(\vec{Q},\omega)$, and $\epsilon_b$ defines a frequency-independent background dielectric constant. In Figs. 2(a) to 2(d) we give some typical polariton dispersions resulting from Eq. (12) for different high-symmetry directions. The polariton branches are given by full lines and labeled *A*, *B*, *C*, and *D*; the exciton dispersion is given by

TABLE VII. Symmetry-adapted two-hole functions for $j_h = (0,2)$. The hole state functions $\Phi_i$, $i=1, \ldots, 4$ have been defined in Eq. 3; quantization axis of the spin states is the [001] direction.

| State and symmetry | $\lvert j_h, m_h\rangle$ | Two-hole representation |
|---|---|---|
| $\Gamma_1$ | $\lvert 0,0\rangle$ | $\frac{1}{2}(\Phi_1^2\Phi_4^4 - \Phi_2^2\Phi_3^4 + \Phi_3^2\Phi_2^4 - \Phi_4^2\Phi_1^4)$ |
| $\Gamma_3^1$ | $\lvert 2,0\rangle$ | $\frac{1}{2}(\Phi_1^2\Phi_4^4 + \Phi_2^2\Phi_3^4 - \Phi_3^2\Phi_2^4 - \Phi_4^2\Phi_1^4)$ |
| $\Gamma_3^2$ | $(\lvert 2,2\rangle + \lvert 2,-2\rangle)/\sqrt{2}$ | $\frac{1}{2}(\Phi_1^2\Phi_2^4 - \Phi_2^2\Phi_1^4 + \Phi_3^2\Phi_4^4 - \Phi_4^2\Phi_3^4)$ |
| $\Gamma_5^1$ | $(\lvert 2,2\rangle - \lvert 2,-2\rangle)/\sqrt{2}$ | $\frac{1}{2}(\Phi_1^2\Phi_2^4 - \Phi_2^2\Phi_1^4 - \Phi_3^2\Phi_4^4 + \Phi_4^2\Phi_3^4)$ |
| $\Gamma_5^2$ | $-(\lvert 2,1\rangle + \lvert 2,-1\rangle)/\sqrt{2}$ | $-\frac{1}{2}(\Phi_1^2\Phi_3^4 - \Phi_3^2\Phi_1^4 + \Phi_2^2\Phi_4^4 - \Phi_4^2\Phi_2^4)$ |
| $\Gamma_5^3$ | $-i(\lvert 2,1\rangle - \lvert 2,-1\rangle)/\sqrt{2}$ | $-\frac{i}{2}(\Phi_1^2\Phi_3^4 - \Phi_3^2\Phi_1^4 - \Phi_2^2\Phi_4^4 + \Phi_4^2\Phi_2^4)$ |

dotted lines. The irreducible representations are indicated. As will be discussed in the next chapter, most of the branches in the different crystal directions can be final states in a hyper-Raman scattering process.

### III. BIEXCITON WAVE FUNCTION AND SELECTION RULES FOR HYPER-RAMAN SCATTERING

The biexciton wave function $|B_J^M(\vec{Q})\rangle$ is classified by the total wave vector $\vec{Q}$, the total angular momentum $J$, and the magnetic quantum number $M$. It is constructed according to Refs. 25–27

$$|B_J^M(\vec{Q})\rangle = \frac{1}{\sqrt{v}}\, e^{i\vec{K}\cdot\vec{R}} F_n^{ij}(\vec{Q})\, |j_e, m_e\rangle |j_h, m_h\rangle , \qquad (13)$$

where $F_n^{ij}$ is the biexciton envelope and $|j_e, m_e\rangle$, $|j_h, m_h\rangle$ are products of Bloch states of two electrons in the conduction band ($\Gamma_6$ symmetry) and of two holes in the valence band ($\Gamma_8$ symmetry), respectively. For simplicity, symmetry-breaking

TABLE VIII. Biexciton wave function in terms of the exciton wave functions of Table I. $P_{AB}$ represents the preceding products with interchanged indices $A$ and $B$.

| State and symmetry | Exciton representation |
|---|---|
| $\Gamma_1$ | $\frac{1}{4\sqrt{2}}(\lvert z\rangle_A\lvert z\rangle_B + \lvert x\rangle_A\lvert x\rangle_B + \lvert y\rangle_A\lvert y\rangle_B - \lvert 2+\rangle_A\lvert 2+\rangle_B + \lvert 2-\rangle_A\lvert 2-\rangle_B - \lvert 20\rangle_A\lvert 20\rangle_B + \lvert 1+\rangle_A\lvert 1+\rangle_B + \lvert 1-\rangle_A\lvert 1-\rangle_B + P_{AB})$ |
| $\Gamma_3^1$ | $\frac{1}{4\sqrt{2}}(-\lvert z\rangle_A\lvert z\rangle_B + \frac{1}{2}\lvert x\rangle_A\lvert x\rangle_B + \frac{1}{2}\lvert y\rangle_A\lvert y\rangle_B - \lvert 2+\rangle_A\lvert 2+\rangle_B + \lvert 2-\rangle_A\lvert 2-\rangle_B + \lvert 20\rangle_A\lvert 20\rangle_B - \frac{1}{2}\lvert 1+\rangle_A\lvert 1+\rangle_B - \frac{1}{2}\lvert 1-\rangle_A\lvert 1-\rangle_B - \sqrt{3}\lvert x\rangle_A\lvert 1+\rangle_B + \sqrt{3}\lvert y\rangle_A\lvert 1-\rangle_B + P_{AB})$ |
| $\Gamma_3^2$ | $\frac{1}{4\sqrt{2}}(-2\lvert 20\rangle_A\lvert 2+\rangle_B + 2\lvert z\rangle_A\lvert 2-\rangle_B - \lvert x\rangle_A\lvert 1+\rangle_B - \frac{\sqrt{3}}{2}\lvert x\rangle_A\lvert x\rangle_B + \frac{\sqrt{3}}{2}\lvert 1+\rangle_A\lvert 1+\rangle_B - \lvert y\rangle_A\lvert 1-\rangle_B + \frac{\sqrt{3}}{2}\lvert y\rangle_A\lvert y\rangle_B - \frac{\sqrt{3}}{2}\lvert 1-\rangle_A\lvert 1-\rangle_B + P_{AB})$ |
| $\Gamma_5^1$ | $\frac{1}{4\sqrt{2}}(2\lvert 20\rangle_A\lvert 2-\rangle_B - 2\lvert z\rangle_A\lvert 2+\rangle_B + i(-\lvert x\rangle_A\lvert 1-\rangle_B + \sqrt{3}\lvert x\rangle_A\lvert y\rangle_B + \sqrt{3}\lvert 1+\rangle_A\lvert 1-\rangle_B + \lvert 1+\rangle_A\lvert y\rangle_B) + P_{AB})$ |
| $\Gamma_5^2$ | $\frac{1}{4\sqrt{2}}(\lvert x\rangle_A\lvert 2+\rangle_B + \sqrt{3}\lvert 1+\rangle_A\lvert 2+\rangle_B + \sqrt{3}\lvert x\rangle_A\lvert 20\rangle_B - \lvert 1+\rangle_A\lvert 20\rangle_B + i(-\lvert y\rangle_A\lvert 2-\rangle_B + \sqrt{3}\lvert 1-\rangle_A\lvert 2-\rangle_B + \sqrt{3}\lvert y\rangle_A\lvert z\rangle_B + \lvert z\rangle_A\lvert 1-\rangle_B) + P_{AB})$ |
| $\Gamma_5^3$ | $\frac{-i}{4\sqrt{2}}(\lvert x\rangle_A\lvert 2-\rangle_B + \sqrt{3}\lvert 1+\rangle_A\lvert 2-\rangle_B + \sqrt{3}\lvert x\rangle_A\lvert z\rangle_B - \lvert z\rangle_A\lvert 1+\rangle_B + i(-\lvert y\rangle_A\lvert 2+\rangle_B + \sqrt{3}\lvert 1-\rangle_A\lvert 2+\rangle_B + \sqrt{3}\lvert y\rangle_A\lvert 20\rangle_B + \lvert 1-\rangle_A\lvert 20\rangle_B) + P_{AB})$ |

effects of the wave vector on the biexciton wave functions are neglected. According to the Pauli principle $|B_J^M(\vec{Q})\rangle$ has to be antisymmetric with respect to exchange of identical particles. Thus, in analogy with the hydrogen molecule,[25,26] the biexciton ground state ($n=0$) is built from the antisymmetric combination of the electron states $(\Gamma_6\otimes\Gamma_6)_-$ and of the hole states $(\Gamma_8\otimes\Gamma_8)_-$ with a symmetric envelope function denoted by $F_0^{+\,+}(\vec{Q})$, having $\Gamma_1$ symmetry. For $\vec{Q}=0$, the biexciton ground state consists according to the decomposition

$$\Gamma_1\otimes(\Gamma_6\otimes\Gamma_6)_-\otimes(\Gamma_8\otimes\Gamma_8)_- = \Gamma_1\otimes\Gamma_1\otimes(\Gamma_1\oplus\Gamma_3\oplus\Gamma_5) \tag{14}$$

of six components with angular momentum $J=0$ and $J=2$ (even-parity states) corresponding to $\Gamma_1$, $\Gamma_3$, and $\Gamma_5$ symmetry. The degeneracy of the biexciton ground state may be lifted due to exchange interaction.[27] The biexciton state vectors are now constructed by forming all products between the antisymmetrized function for two electrons (upper index, 1,3)

$$|0,0\rangle_e = (1/\sqrt{2})(\alpha^1\beta^3 - \alpha^3\beta^1) \tag{15}$$

and the antisymmetrized functions for two holes (upper index 2,4) of Table VII. Subsequently, we transform to the exciton representation by using the symmetrized exciton functions of Table I. The result is given in Table VIII.

In order to study the selection rules for dipole transitions, the easiest way is to neglect all polariton effects. Then the probability for the hyper-Raman process is given by[28]

$$P_n(\vec{q},\vec{k},\vec{q}_l) = \frac{2\pi}{\hbar}\left|\sum_{M,n'}\sum_{\vec{K},\vec{Q}}\frac{\langle\psi^n(\vec{k})|H_I^e(\vec{q})|B_J^M(\vec{K})\rangle\langle B_J^M(\vec{K})|H_I^a(\vec{q}_l)|\psi^{n'}(\vec{Q})\rangle}{[E_B^M(\vec{K})-2\hbar\omega_{\vec{q}_l}][E_x^{n'}(\vec{Q})-\hbar\omega_l]}\langle\psi^{n'}(\vec{Q})|H_I^a(\vec{q}_l)|0\rangle\right|^2\delta(E_x^n(\vec{k})+\hbar\omega_q-2\hbar\omega_{q_l}). \tag{16}$$

Thereby $|0\rangle$ denotes the crystal ground state, $|\psi^{n'}(\vec{Q})\rangle$, $E_x^{n'}(\vec{Q})$ the state vector and energy of an exciton state and $|B_J^M(\vec{K})\rangle$, $E_B^M(\vec{K})$ the state vector and energy of the biexciton. $H_I^a(\vec{q}_l)$ and $H_I^e(\vec{q})$ are the electron-photon interaction for absorption of a laser photon $(\vec{q}_l,\omega_{\vec{q}_l})$ and emission of a photon $(\vec{q},\omega_{\vec{q}})$, which is observed.

From Eq. (16) together with Table VIII we obtain the selection rules if we consider the ground-state symmetry ($\Gamma_1$) and the transformation properties of the interaction operator which in the dipole approximation is $\Gamma_5$. Since we do not want to calculate intensities, we do not consider interference due to the sum over intermediate states in Eq. (16). The hyper-Raman process is dipole-allowed only if all three matrix Eq. (16) are nonzero.

To exemplify the procedure let us discuss the case when all wave vectors $\vec{q}_l,\vec{k}$, and $\vec{q}$ are parallel to the [001] crystal direction and that the laser photons are polarized parallel to [100]. In this case $H_I^a(\vec{q}_l)$ transforms as the coordinate $x$ and allows the transition to the exciton state $|x\rangle$. With two of these laser photons, consequently, we can excite the two-exciton state $|x\rangle_A|x\rangle_B$ which is part of the biexcitons with symmetry $\Gamma_1$, $\Gamma_3^1$, and $\Gamma_3^2$ (Table VIII). Considering for the final emission process the two independent polarizations parallel to [100] and [010] (transforming as $x$ and $y$, respectively) we obtain for the different intermediate biexcitons ($\Gamma_1$, $\Gamma_3^1$, $\Gamma_3^2$) the final states of Table IX. These final states belong to the irreducible representations $\Delta_3$, $\Delta_4$ [c.f. Table III and Eq. (8)], which are degenerate and yield two different solutions, which we expect to show up as two different hyper-Raman lines in experiment.

The biexciton wave functions of Table VIII can also be used to calculate selection rules for biexciton luminescence. For this case, we do not have to consider the excitation process, but instead to assume the biexciton states to be occupied and discuss the emission of one photon of polarization [100] or [010]. According to the dipole selection rules those emission processes are possible for which the initial biexciton contains, respectively, $|x\rangle_A|\lambda\rangle_B$ or $|y\rangle_A|\lambda\rangle_B$ as a component. Then, the final exciton state $|\lambda\rangle$ is left behind in the crystal. In Table IX we give all selection rules for luminescence and hyper-Raman scattering.

TABLE IX. Selection rules for luminescence and hyper-Raman scattering, all wave vectors being along [001].

| Biexciton state | Polarization of exciting photons ∥ [100] | ∥ [010] | Polarization of emission ∥ [100] | ∥ [010] |
|---|---|---|---|---|
| $\Gamma_1$ | $a$ | $a$ | $\|x\rangle$ | $\|y\rangle$ |
| $\Gamma_3^1$ | $a$ | $a$ | $\|x\rangle$, $\|1+\rangle$ | $\|y\rangle$, $\|1-\rangle$ |
| $\Gamma_3^2$ | $a$ | $a$ | $\|x\rangle$, $\|1+\rangle$ | $\|y\rangle$, $\|1-\rangle$ |
| $\Gamma_5^1$ | $f$ | $f$ | $\|y\rangle$, $\|1-\rangle$ | $\|x\rangle$, $\|1+\rangle$ |
| $\Gamma_5^2$ | $f$ | $f$ | $\|20\rangle$, $\|2+\rangle$ | $\|2-\rangle$, $\|z\rangle$ |
| $\Gamma_5^3$ | $f$ | $f$ | $\|2-\rangle$, $\|z\rangle$ | $\|2+\rangle$, $\|20\rangle$ |

$a$: hyper-Raman allowed.
$f$: hyper-Raman forbidden.

TABLE X. Selection rules for luminescence and hyper-Raman scattering, all wave vectors being along [110].

| Biexciton state | Polarization of exciting photons [$\bar{1}10$] | [001] | Polarization of emission [$\bar{1}10$] | [001] |
|---|---|---|---|---|
| $\Gamma_1$ | $a$ | $a$ | $\|x\rangle'$ | $\|y\rangle'$ |
| $\Gamma_3^1$ | $a$ | $a$ | $\|x\rangle',\|1+\rangle'$ | $\|y\rangle'$ |
| $\Gamma_3^2$ | $f$ | $f$ | $\|2-\rangle',\|z\rangle'$ | $\|20\rangle',\|2+\rangle'$ |
| $\Gamma_5^1$ | $a$ | $f$ | $\|x\rangle',\|1+\rangle'$ | $\|1-\rangle'$ |
| $\Gamma_5^2$ | $f$ | $f$ | $\|y\rangle',\|1-\rangle',\|2+\rangle'$ | $\|x\rangle',\|1+\rangle',\|2-\rangle',\|z\rangle'$ |
| $\Gamma_5^3$ | $f$ | $f$ | $\|y\rangle',\|1-\rangle',\|2+\rangle'$ | $\|x\rangle',\|1+\rangle',\|2-\rangle',\|z\rangle'$ |

$a$: hyper-Raman allowed.
$f$: hyper-Raman forbidden.

In Table X we present the selection rules in the case where wave vectors $\vec{q}_l$, $\vec{q}$, and $\vec{k}$ are parallel to the [110] direction. In this case the polarizations parallel to [$\bar{1}10$] or [001] lead to states of $\Sigma_2$ or $\Sigma_1$ symmetry, respectively. Thus for a given polarization of the emitted light all final states in the hyper-Raman process have the same symmetry.

If the wave vectors are along the [111] direction, the possible final states belong to the twofold representation $\Lambda_3$ and the hyper-Raman (HR) spectra do not change with changing the polarization of the emitted light. Therefore, no selection rules are calculated for this case. For experimental configurations different from those given above, the hyper-Raman selection rules can be obtained with the help of Table VIII.

## IV. EXPERIMENTAL RESULTS

The HR scattering of CuBr has been measured with the experimental setup shown in Fig. 3. The exciting source was a tunable dye laser using a solution of $2\times10^{-3}$ mol/l of carbostyril 3 in ethanol as an active medium and pumped transversely by a 1M50A Lambda Physik nitrogen laser. Two different types of laser cavities have been successively used: In the first one, the tuning elements were a grating in a Littrow mount with an expanding beam telescope and an additional compact Fabry-Perot.[29] A spectral emission linewidth of 0.2 meV was obtained in the spectral range of 2.920 to 2.980 eV. In the second one, the only tuning element was a grating working at grazing incidence.[30,31] The spectral width obtained with this simpler setup was equal to the preceding one.

The duration of the dye laser pulse was 1.2 ns. The beam was spatially filtered by a diaphragm and polarized by a Glan prism. Its intensity could be varied by a set of neutral filters. Its stability was checked during the experiment by recording its intensity with an UVHC 20 Photocell, the signal of which was fed through Ortec Amplifiers and integrated in an ATNE boxcar.

The dye laser beam was focused on the sample. The size of the illuminated spot was about 50 $\mu$m. The maximum intensity impinging on the crystal surface was several MW/cm$^2$. By means of a pivoting optical bench on which a rotating mirror, the focusing lens, and the Glan polarizer were mounted, the angle $\alpha$ between the laser beam and the normal to the crystal surface could be varied (Fig. 4).

The samples were high-quality monocrystals grown by a vapor phase method. They were cooled down to liquid-helium temperature in a quartz double Dewar. It was possible to study the

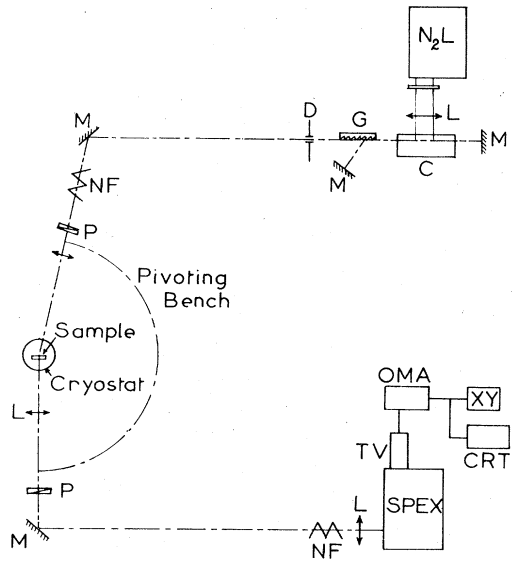


FIG. 3. Experimental setup for measuring the hyper-Raman scattering.

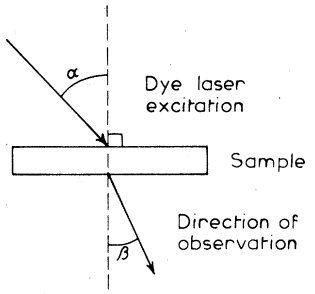


FIG. 4. Forward-scattering configuration with variable angles for incident $\alpha$ and emitted light $\beta$.

scattering in a backward configuration, the illuminated surface on the sample being directly observed, or, in a forward configuration, the emission transmitted through the sample being recorded. The light emitted in a direction making an angle $\beta$ with the normal of the crystal surface, analyzed through a Polaroid polarizer, was focused on the entrance slit of a $\frac{3}{4}$ m Spectrograph Spex used in the second order. The spectra were recorded by means of an Optical Multichannel Analyzer (OMA) (Par 1205D). They were visualized on an oscilloscope and registered on an XY recorder.

The overall precision of the absolute measurements of the spectral positions was 0.12 meV; that of the relative measurements better than 0.04 meV. This precision was reached by keeping the spectrograph grating in the same position during the whole experiment and by a precision wavelength calibration of the OMA, using the spectrum of an argon lamp (4200.67 and 4190.71 Å) and of a neon lamp (8377.607 Å) as well as the interference fringes of a Fabry-Perot illuminated by the white light of a tungsten lamp.

The hyper-Raman emission from the (110) surface of cleaved samples of CuBr has been first measured in a backward configuration ($\alpha = 23°$, $\beta = 2°$). Figure 5 shows typical HR emission spectra obtained at 4.2 K for two different polarizations of the emitted light $\vec{e} \parallel [\bar{1}10]$ and $\vec{e} \parallel [001]$. The exciting laser beam has its polarization vector $\vec{e}_i \parallel [110]$ and its photon energy is close to half the $\Gamma_1$ biexciton energy. Different emission lines $R_T$, $R_t$, $S$, and $N_L$ are observed. Some diffused laser light is also recorded.

In Fig. 6, we have plotted the spectral positions of the HR lines as functions of the exciting photon energies $\hbar\omega_i$ for different polarizations. The $R_T$ line is observed in both polarizations with a small but definite energy difference between the two corresponding spectral positions. This line is detected near half the energy of all the biexciton resonances[32] [$\frac{1}{2}E_B(\Gamma_1) = 2.9530$ eV, $\frac{1}{2}E_B(\Gamma_5) = 2.9551$ eV, $\frac{1}{2}E_B(\Gamma_3) = 2.9564$ eV]. The $R_t$ line is observed at identical spectral positions for both polarizations near all the biexciton resonances. The $S$ line is recorded only in the $\vec{e} \parallel [001]$ polarization, as it is also seen in Fig. 5 near the $\Gamma_1$ and $\Gamma_5$ biexciton resonances. The $T$ line is weakly observed for both polarizations but only near the $\Gamma_3$ biexciton

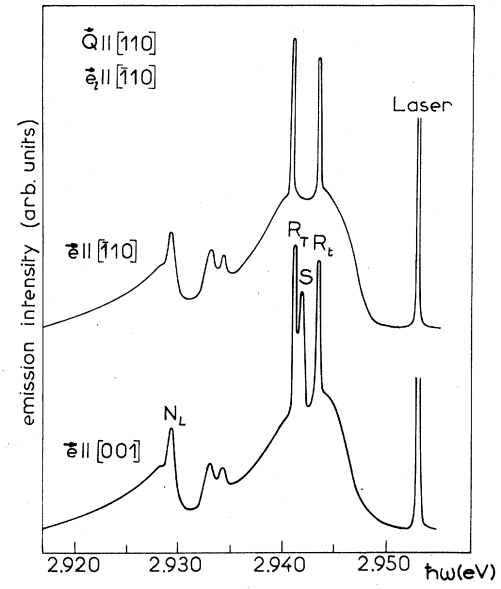


FIG. 5. Typical backward emission spectra for $\vec{Q} \parallel [110]$ and different polarizations. The different lines are discussed in the text.

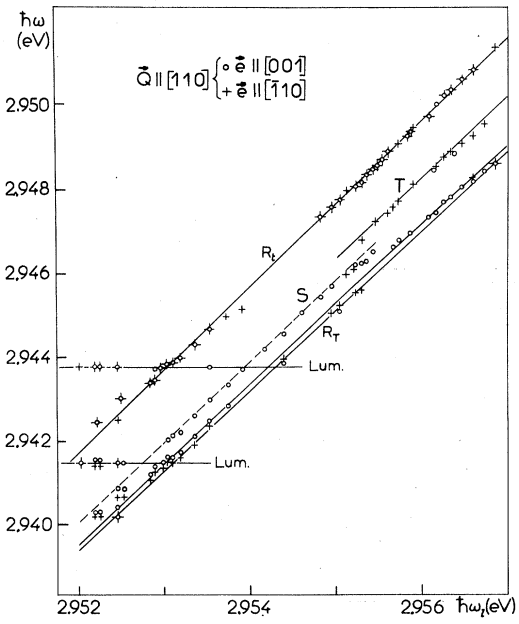


FIG. 6. Position of luminescence and hyper-Raman lines as function of incident laser energy for $\vec{Q} \parallel [110]$.

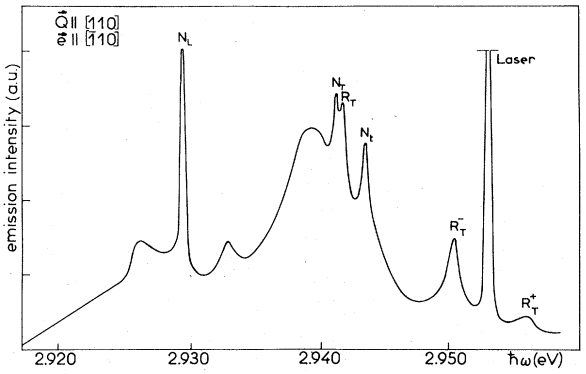


FIG. 7. Typical forward emission spectrum for $\vec{Q} \| [110]$ and polarization $\vec{e} \| [110]$ observed with $\alpha = 37°$ and $\beta = 0°$. The different lines are discussed in the text.

resonance. All these lines shift almost linearly with $\hbar\omega_t$ with a slope of 2.0. The other lines called $N_L$, $N_T$, and $N_t$, recorded respectively at 2.9293, 2.9415, and 2.9438 eV, remain at the same spectral positions when the exciting laser is tuned. They are related to a luminescence process.

The HR emission of these cleaved samples has also been studied in a forward configuration ($\alpha = 23°$, 37°, and 45°, $\beta = 0°$). The thickness of the platelets used was about 300 $\mu$m. Figure 7 shows an HR spectrum for $\alpha = 37°$ and $\beta = 0°$ at 4.2 K. The exciting laser beam is polarized parallel to the [001] axis. The energy of its photons is 2.9529 eV. The emitted light is measured in $\vec{e} \| [\bar{1}10]$ polarization. The spectrum is identical in the $\vec{e} \| [001]$ polarization. On both sides of the laser line, two new lines $R_T^+$ and $R_T^-$ are observed. The photon energy of the laser being at the $\Gamma_1$ biexciton resonance, the luminescence lines $N_T$, $N_t$, and $N_L$ are also obtained. An additional HR emission line, corresponding to the $R_t$ line observed in backward-scattering configuration, can also be seen. In Fig. 8 we have plotted the spectral position of the $R_T^+$ and $R_T^-$ lines for the two different angles of incidence $\alpha$ of the exciting laser beam. The $R_t$ line observed with this configuration is at the same spectral position for the two incident angles as seen in this figure.

We have also studied the $R_L$ line in a backward-scattering configuration ($\alpha = 30°$, $\beta = 60°$). In Fig. 9, the spectral position of this line is plotted as a function of the exciting photon energy. The emission was polarized in the (001) plane. The scattering angle in this configuration was taken to be less than 180° in order to have a detectable $R_L$ emission, as discussed for CuCl in Ref. 33. The wave vector of the polariton left in the crystal was at first kept almost parallel to the [110] crystal

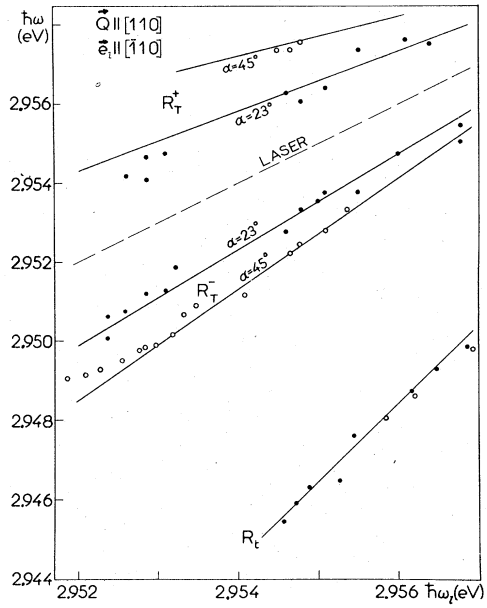


FIG. 8. Position of emission lines in forward configuration as function of the incident laser energy. The angle $\alpha$ between incident light and the [110] direction are indicated. The emitted light was observed almost parallel to [110]. The line position does not depend on the polarization vector $\vec{e}$.

direction, then changed by about 25° towards the [111] and [001] directions by varying $\alpha$ and $\beta$. No spectral shift of the $R_L$ line could be measured at a fixed exciting photon energy.

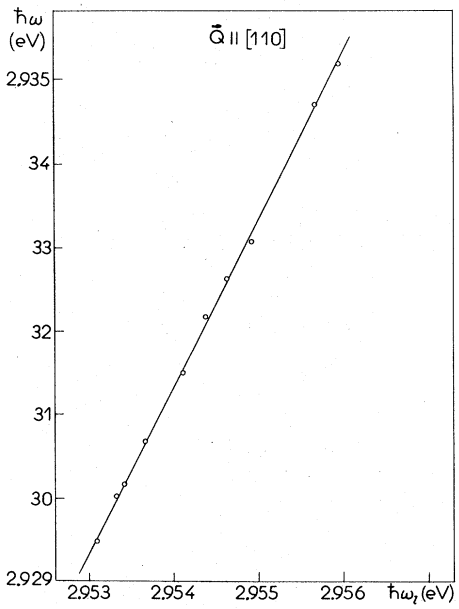


FIG. 9. Position of the $R_L$ emission line in a backward configuration as a function of the incident laser energy ($\alpha = 30°$, $\beta = 60°$).

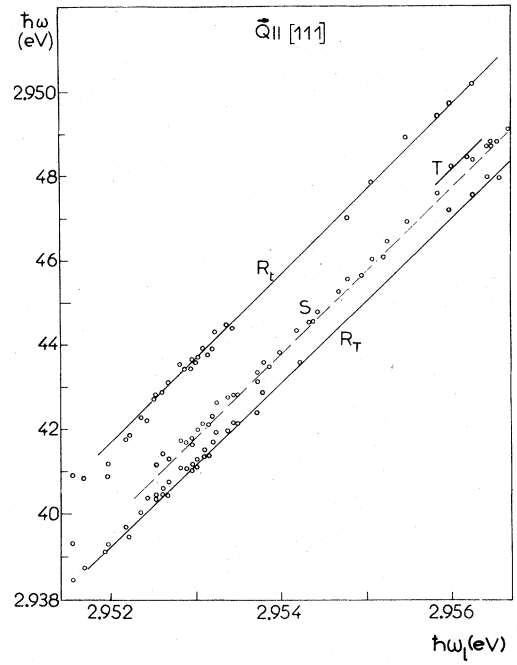


FIG. 10. Position of emission lines for $\vec{Q}$ ∥ [111] as function of incident laser energy.

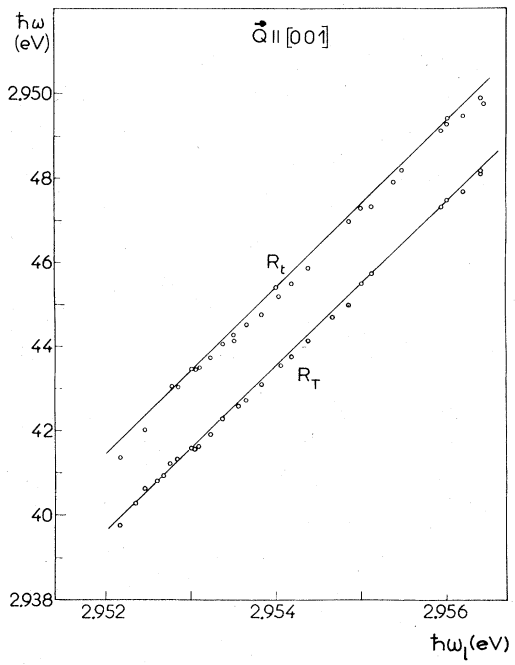


FIG. 11. Position of emission lines for $\vec{Q}$ ∥ [001] as function of incident laser energy.

The $R_L$ emission could also be observed in a forward configuration. The scattering angle $\theta$ has to be different from zero in order to detect this emission.[33] A small shift of the line towards higher spectral positions ($0.08 \pm 0.02$ meV) was measured in this configuration as compared to the backward configuration. It was important that no stimulated $R_L$ emission took place.

The HR emission of CuBr has also been measured for other crystallographic directions in a backward-scattering configuration. We have obtained [111]- and [001]-oriented surfaces of CuBr by cutting our crystals with a string saw, by polishing them, and finally etching the surfaces with a solution of bromhydric acid in aceton. The HR emission was only observed with surfaces of perfect optical quality.

In Fig. 10, we have plotted the spectral positions of the HR emission lines scattered in a backward configuration by a (111) surface as functions of the photon energies of an exciting laser polarized parallel to $[\bar{1}\bar{1}2]$. These positions are independent of the polarization of the emitted light. The $R_T$ and $R_t$ lines are observed only close to the $\Gamma_1$ and $\Gamma_3$ biexciton resonances. The $S$ line is detected near the three resonances. All these lines shift almost linearly with $\hbar\omega_l$ with a slope of 2.0.

In Fig. 11, the spectral positions of the HR emission lines, scattered in a backward configuration from a (001) surface, are plotted as functions of the photon energies of an exciting laser polarized parallel to [010]. The $R_T$ and $R_t$ are observed near the three biexciton resonances. They again shift linearly with $\hbar\omega_l$, the slope being equal to 2.0. Again, the line position is independent of the polarization vector of the emitted and exciting light.

## V. DISCUSSION

Let us first discuss the experimental results obtained from observation along the [110] direction with the incident light being polarized parallel to $[\bar{1}10]$. This corresponds to the experimental data of Figs. 5 and 6. According to the selection rules (Table X) and the exciton matrix (Table V) the final states of the scattering process have symmetry $\Sigma_1$ or $\Sigma_2$ if the emitted light is polarized parallel to [001] or $[\bar{1}10]$, respectively. In the first case ($\Sigma_1$) the final state left in the crystal is $|y\rangle'$ (Table X) which, due to the $\vec{Q}$-dependent coupling (Table V) mixes with all the other states of $\Sigma_1$ symmetry.

Due to the large splitting between the $\Gamma_{5L}$ and $\Gamma_{5T}$ states ($\Delta_{LT}$) at $\vec{Q}=0$, there is almost no admixture of the $|y\rangle'$ state into the longitudinal exciton at the wave vectors under consideration. A hyper-Raman line corresponding to the state $|z\rangle'$ as one of the final polariton states is unlikely to be detected in the experiment. We expect three

hyper-Raman lines corresponding to the decay of the virtually excited biexciton into pairs of polaritons $(A_1, A_i)$, $i=1,2,3$ [Fig. 2(b)]. Four lines are seen, however, in Fig. 6, but the line $T$ was observed only in a small energy range of the exciting laser. These lines are interpreted as follows: $R_t$ corresponds to a final pair of polariton states $(A_1, A_1)$, $T$ to $(A_1, A_2)$, $R_T$ to $(A_1, A_3)$. The line $S$ may only be explained by a stimulated emission in the crystal surface which is diffused from the sample surface to the spectrograph similar to the one observed in CuCl.[34] The final-state wave vector $\vec{k}$ has then some arbitrary direction in the (001) plane. The hyper-Raman line $(R_L)$ corresponding to a final pair $(A_1, A_4)$ is missing in the experimental configuration of Figs. 5 and 6. Instead we have chosen a different configuration to observe the $R_L$ line. According to Ref. 33 the $R_L$ line can be seen for $\hbar\omega_l$ being close to half the $\Gamma_1$ biexciton energy if the scattering angle $\theta$ between $\vec{q}_l$ and $\vec{q}$ is near 60° and the polarization of the emitted light is in the scattering plane (001). For this experiment the wave vector of the longitudinal exciton was first kept parallel to the [110] direction. Then its direction was turned towards the [100] and [111] directions, in order to study warping effects.

In the forward-scattering configuration (Figs. 7 and 8), the hyper-Raman lines $R_T^+$ and $R_T^-$ were observed which correspond to transitions with both final states on the lower branch $(A_1, A_1)$ but with different wave vector combinations. As discussed in Ref. 32 in more detail, three scattering channels exist for one given scattering angle $\theta < 30°$, two of which are observed in the experiment. The $R_t$ line of Fig. 8 is interpreted as before as being due to a final pair $(A_1, A_3)$.

The $R_L$ line [final pair $(A_1, A_4)$] was also observed in forward scattering configuration. A detailed analysis of the experimental data gives for the $R_L$ line an energy which is $\Delta E_L = 0.08 \pm 0.02$ meV higher than in the backward-scattering configuration for the same exciting photon energy. This energy difference is attributed to the curvature of the longitudinal exciton band as for CuCl in Ref. 15.

The experimental data allow one to calculate from the law of energy conservation Eq. (2) the energy $E_j(\vec{k})$ of the final state, which is not observed. With this information on the energies we determined the wave vectors $\vec{q}$ and $\vec{k}$ [Eq. (1)], the

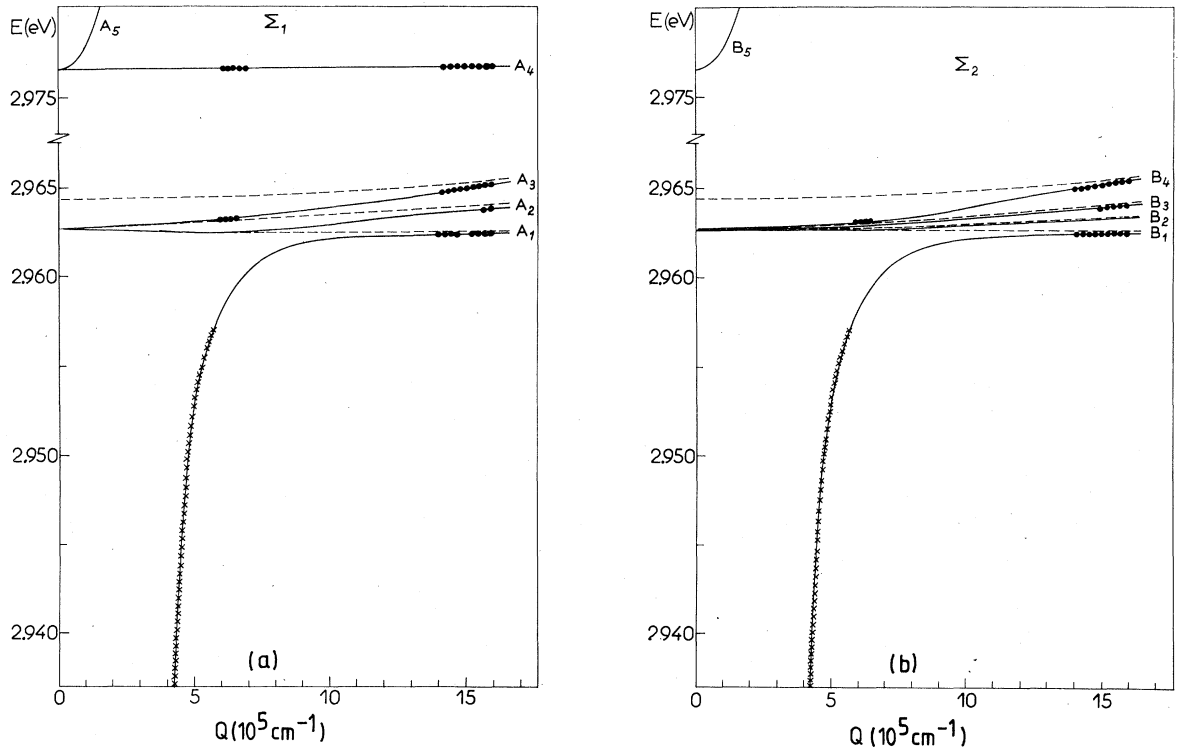


FIG. 12. Calculated polariton dispersion (full lines) and experimental data for $\vec{Q} \| [110]$. Observed hyper-Raman data (×) and the polariton dispersion are used to fix the wave vector of the second polariton (●) which result from the decay of the biexciton. The dispersion of the corresponding excitons is given by the dashed lines. (a) Polariton branches with $\Sigma_1$ symmetry observed with polarization parallel to [001]. (b) Polariton branches with $\Sigma_2$ symmetry observed with polarization parallel to $[\bar{1}10]$.

scattering angles $\theta$, and the refractive index $n(\vec{q},\omega)$ from the polariton dispersion Eq. (12) in a self-consistent way.[34,35] Using the experimental data discussed so far, together with the fact that no directional dependence (warping) of the longitudinal exciton mass could be detected in our experiment, we determine some of the free parameters of the multicomponent system which are given below. The obtained fit is shown in Figs. 6, 8, and 12(a).

The observed isotropy of the longitudinal exciton mass $M_{ex}^{L}$ can be discussed in terms of the exciton matrices of Tables III, V, and VI. Due to the large splitting $E(\Gamma_{5L})-E(\Gamma_3+\Gamma_4)=\Delta_{ST}+\Delta_{LT}=13.9$ meV and the small $Q$ values involved ($|\vec{Q}|\leq 15\times10^5$ cm$^{-1}$) the coupling between the longitudinal and triplet excitons via $\vec{Q}$-linear term is considered as perturbation. We obtain the linearly dependent relations

$$\frac{\hbar^2}{2M_{ex}^{L}}=G_1-\tfrac{5}{2}\delta_1-G_2+\tfrac{1}{3}\delta_2+\frac{3C_Q^2}{4(\Delta_{ST}+\Delta_{LT})},\quad \vec{Q}\parallel[001]$$

$$\frac{\hbar^2}{2M_{ex}^{L}}=G_1-\tfrac{5}{2}\delta_1-\tfrac{1}{4}G_2+\tfrac{1}{12}\delta_2-\tfrac{3}{4}G_3+\tfrac{1}{4}\delta_3+\frac{3C_Q^2}{16(\Delta_{ST}+\Delta_{LT})},\quad \vec{Q}\parallel[110] \qquad (17)$$

$$\frac{\hbar^2}{2M_{ex}^{L}}=G_1-\tfrac{5}{2}\delta_1-G_3+\tfrac{1}{3}\delta_3,\quad \vec{Q}\parallel[111].$$

If we do not consider for the moment $\vec{Q}$-dependent exchange terms ($\delta_i=0$, $i=1,2,3$), we can check the validity of the band parameters for CuBr which were obtained more recently from the fine structure of excitonic 2P states.[36] Using the Luttinger parameters $\gamma_1'=\gamma_1+m_0/m_e=5.7$, $\gamma_2=0.2$, and $\gamma_3=0.56$ from Ref. 36 and the electron mass $m_e/m_0=0.22$ we calculate from Eq. (9) $G_1=0.69\hbar^2/2m_0$, $G_2=0.25\,\hbar^2/2m_0$, and $G_3=0.71\,\hbar^2/2m_0$ ($m_0$ is the free electron mass). These parameters yield a strong warping of the longitudinal exciton band with a negative curvature for $\vec{Q}\parallel[111]$. There are several possibilities to explain this unreasonable result: (1) The band parameters of Ref. 36 must be corrected due to the $k$-linear term which was not considered in analyzing the fine structure of the 2P states. (2) The influence of the electron-phonon interaction on the excited exciton states studied in Ref. 36 is different from that on the exciton ground state. (3) The $\vec{Q}$-dependent exchange terms compensate most of the warping effects. Since the information provided by the HR experiment is restricted to small $Q$ values, we were not able to give a final solution to this problem. It was possible, however, to fit all experimental data by assuming $G_2=G_3=0$, $\delta_2=\delta_3=0$, $G_1=0.69\,\hbar^2/2m_0$ and determined $\delta_1$ from Eq. (17) by neglecting the influence of the $\vec{Q}$-linear term on the longitudinal exciton dispersion, which is of the order of the experimental accuracy of $M_{ex}^{L}=11\pm3\ m_0$. We thus obtain from the HR data for $\vec{Q}\parallel[110]$

$$E(\Gamma_{5L})=2976.6\pm0.1\ \text{meV},$$

$$E(\Gamma_{5T})=2964.4\pm0.2\ \text{meV},$$

$$E(\Gamma_3+\Gamma_4)=2962.7\pm0.2\ \text{meV},$$

$$\Delta_2\leq 7\times10^{-2}\ \text{meV},$$

$$C_Q=(73\pm4)\times10^{-8}\ \text{meV cm},$$

$$\epsilon_b=5.4\pm0.2,$$

$$\delta_1=(0.24\pm0.02)\hbar^2/2m_0.$$

A splitting of the $\Gamma_3$ and $\Gamma_4$ excitons [$E(\Gamma_4)-E(\Gamma_3)=3\Delta_2$] is estimated to be smaller than 0.2 meV and could not be detected within our experimental accuracy. It was, therefore, neglected in our analysis. The value of $C_Q$ is in good agreement with those given by Khan,[37] Suga *et al.*,[2] and Fiorini *et al.*[9] The most recent reflectivity measurements of Ref. 9 support the above discussion of the mass and exchange parameters, since there, also, no indication of warping was obtained. In addition, an isotropic mass parameter was used for the triplet exciton states which is in agreement with our result and with that of Ref. 38. As a cross check on the derived set of parameters we

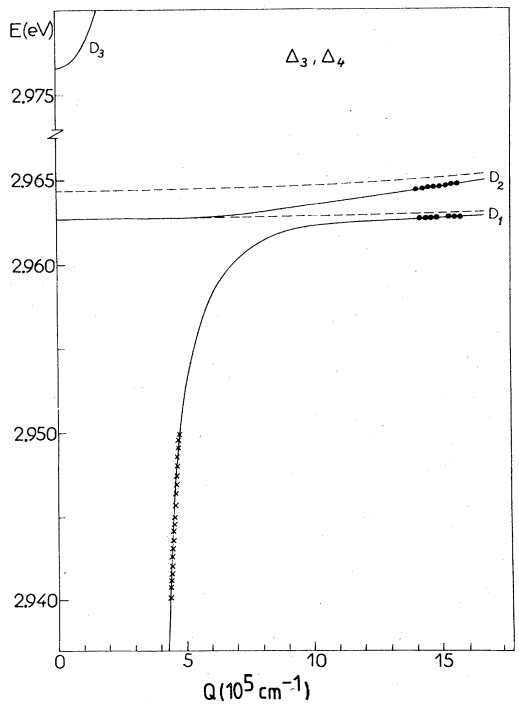


FIG. 13. Calculated polariton dispersion and experimental data for $\vec{Q}\parallel[001]$. Notation as in Fig. 12.

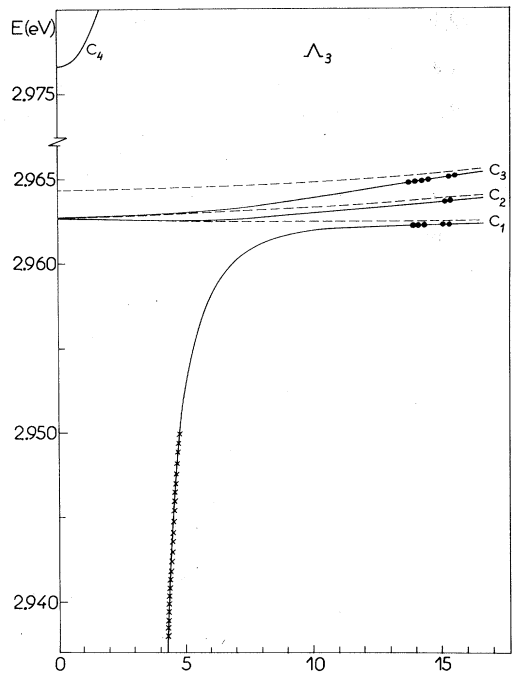


FIG. 14. Calculated polariton dispersion and experimental data for $\vec{Q} \| [111]$. Notation as in Fig. 12.

calculated the energies of the hyper-Raman lines for the other scattering configurations presented in Sec. IV without any further adjustable parameter. The calculated energies were used to draw the solid lines in Figs. 8, 9, 10, and 11, which agree nicely with the experimental data. The energy of the experimental hyper-Raman lines together with the energy of the final state partner and their corresponding wave vectors, as calculated from the polariton dispersion, are visualized in Figs. 12(b), 13, and 14 to demonstrate the consistency of the polariton model and the reliability of the derived parameter set.

Since the HR experiment is sensitive to the polariton dispersion at small $Q$ values, it allows one to determine in particular the exchange splittings $(\Delta_{ST}, \Delta_{LT})$ at $Q=0$ and the $\vec{Q}$-linear term. The parameter values for $G_2$, $G_3$, $\delta_2$, and $\delta_3$ can be obtained from the polariton dispersion at larger $\vec{Q}$ values, which can be studied by resonant Brillouin scattering. Thus a complete set of parameters can be determined when Brillouin scattering data are available.

## VI. CONCLUSIONS

We have shown in this paper that hyper-Raman scattering is a good tool to determine the dispersion of multicomponent excitonic polaritons in the bottleneck region, if one or more intermediate biexciton states enhance the transition probability. In this context, it is very important that not only the energy of dipole-active states may be obtained, but also longitudinal exciton states and triplet excitons may be one of the final states in the scattering process. In addition, we were able to obtain experimental results on the polariton dispersion in different crystal directions.

A detailed analysis of the experimental data yields direct evidence on interaction between the different exciton states, on the exciton mass parameters, and gives a strong hint on the wave vector dependence of the exchange interaction. We expect, that the method proposed here will also work in other semiconductors with zinc-blende structure.

## ACKNOWLEDGMENTS

The support of this work by an A.T.P. of the C.N.R.S. and by the Deutsche Forschungsgemeinschaft is thankfully acknowledged. One of the authors (U.R.) is also indebted to the DAAD for financial support of a stay in Strasbourg, during which the paper was brought to its final version.

## APPENDIX

In order to formulate the center-of-mass Hamiltonian, we first form symmetrized expressions of the electron-spin operator $\sigma_x$, $\sigma_y$, $\sigma_z$, of the hole-spin operators $J_x$, $J_y$, $J_z$, and of the components of the center-of-mass wave vector $Q_x$, $Q_y$, $Q_z$. While $\sigma_i$ and $J_i$ transform as $\Gamma_4$, $Q_i$ transforms as $\Gamma_5$. Using the Tables of Ref. 23 we obtain up to second order in $Q_i$:

$\Gamma_1$: $Q^2$; $1_e$; $1_h$

$\Gamma_2$: $J_x J_y J_z$

$\Gamma_3$: $3Q_z^2 - Q^2, \sqrt{3}(Q_x^2 - Q_y^2)$; $3J_z^2 - J^2, \sqrt{3}(J_x^2 - J_y^2)$

$\Gamma_4$: $\sigma_x, \sigma_y, \sigma_z$; $J_x, J_y, J_z$; $J_x^3, J_y^3, J_z^3$

$\Gamma_5$: $Q_x, Q_y, Q_z$; $Q_y Q_z, Q_z Q_x, Q_x Q_y$;

$\{J_y, J_z\}, \{J_z, J_x\}, \{J_x, J_y\}$;

$\{J_x, J_y^2 - J_z^2\}, \{J_y, J_z^2 - J_x^2\}, \{J_z, J_x^2 - J_y^2\}$.

To make the operator act in the eightfold space of the exciton ground state, we have to combine the symmetrized expressions in $\underline{\sigma}$ with those in $\underline{J}$ using again Ref. 23. Finally, we form products of these combinations with the symmetrized $\vec{Q}$ expressions, having the same symmetry. Thus we obtain the desired terms which are fully invariant under the symmetry operations of $T_d$. Since the Hamiltonian has also to be invariant with respect to time inversion, we drop all invariants which consist of odd powers in $\vec{Q}$, $\underline{\sigma}$, and $\underline{J}$. The resulting invariants are: $\vec{Q}$-independent exchange terms

$$1_e \otimes 1_h;\ \underline{\sigma}\cdot\underline{J};\ \sigma_x J_x^3 + \sigma_y J_y^3 + \sigma_z J_z^3; \tag{A1}$$

$\vec{Q}$-dependent exchange terms

1. $Q_x\sigma_x(J_y^2 - J_z^2) + Q_y\sigma_y(J_z^2 - J_x^2) + Q_z\sigma_z(J_x^2 - J_y^2)$,
2. $Q_x(\sigma_y\{J_x, J_y\} - \sigma_z\{J_z, J_x\}) + Q_y(\sigma_z\{J_y, J_z\} - \sigma_x\{J_x, J_y\}) + Q_z(\sigma_x\{J_x, J_y\} - \sigma_y\{J_y, J_z\})$,
3. $\vec{Q}^2\underline{\sigma}\cdot\underline{J}$,
4. $\vec{Q}^2(\sigma_x J_x^3 + \sigma_y J_y^3 + \sigma_z J_z^3)$,
5. $Q_x^2\sigma_x J_x + Q_y^2\sigma_y J_y + Q_z^2\sigma_z J_z$,
6. $Q_x^2\sigma_x J_x^3 + Q_y^2\sigma_y J_y^3 + Q_z^2\sigma_z J_z^3$,
7. $(Q_y^2 - Q_z^2)\sigma_x\{J_x, J_y^2 - J_z^2\} + (Q_z^2 - Q_x^2)\sigma_y\{J_y J_z^2 - J_x^2\} + (Q_x^2 - Q_y^2)\sigma_z\{J_z, J_x^2 - J_y^2\}$,
8. $Q_yQ_z(\sigma_y J_z + \sigma_z J_y) + Q_zQ_x(\sigma_x J_z + \sigma_z J_x) + Q_xQ_y(\sigma_x J_y + \sigma_y J_x)$,
9. $(Q_yQ_z\sigma_x + Q_zQ_x\sigma_y + Q_xQ_y\sigma_z)J_xJ_yJ_z$,
10. $Q_yQ_z(\sigma_y J_z^3 + \sigma_z J_y^3) + Q_zQ_x(\sigma_z J_x^3 + \sigma_x J_z^3) + Q_xQ_y(\sigma_x J_y^3 + \sigma_y J_x^3)$,
11. $Q_yQ_z(\sigma_y\{J_z, J_x^2 - J_y^2\} - \sigma_z\{J_y, J_z^2 - J_x^2\}) + Q_zQ_x(\sigma_z\{J_x, J_y^2 - J_z^2\} - \sigma_x\{J_z, J_x^2 - J_y^2\}) + Q_xQ_y(\sigma_x\{J_y, J_z^2 - J_x^2\} - \sigma_y\{J_x, J_y^2 - J_z^2\})$, (A2)

and finally nonexchange terms

1. $(Q_x\{J_x, J_y^2 - J_z^2\} + Q_y\{J_y, J_z^2 - J_x^2\} + Q_z\{J_z, J_x^2 - J_y^2\}) \otimes 1_e$,
2. $Q^2 1_e \otimes 1_h$, (A3)
3. $[Q_x^2(J_x^2 - \frac{1}{3}J^2) + Q_y^2(J_y^2 - \frac{1}{3}J^2) + Q_z^2(J_z^2 - \frac{1}{3}J^2)] \otimes 1_e$,
4. $(Q_yQ_z\{J_y, J_z\} + Q_zQ_x\{J_z, J_x\} + Q_xQ_y\{J_x, J_y\}) \otimes 1_e$.

Out of these invariant expressions only those of (A1) and (A3) have been considered in previous work (see, e.g., Ref. 1). The $\vec{Q}$-dependent exchange terms correspond to the $\vec{Q}$ dependence of the Bloch functions in the exchange integral.

*Present address: Max-Planck-Institut für Festkörperforschung D-7000 Stuttgart 80, Bundesrepublik Deutschland.

[1]K. Cho, Phys. Rev. B 14, 4463 (1976).
[2]S. Suga, K. Cho, and M. Bettini, Phys. Rev. B 13, 943 (1976).
[3]E. O. Kane, Phys. Rev. B 11, 3850 (1975).
[4]J. M. Luttinger, Phys. Rev. 102, 1030 (1956).
[5]G. Dresselhaus, Phys. Rev. 100, 580 (1955).
[6]J. J. Hopfield, Phys. Rev. 112, 1555 (1958).
[7]S. I. Pekar, Zh. Eksp. Teor. Fiz. 33, 1022 (1957) [Sov. Phys.—JETP 6, 785 (1958)].
[8]S. Suga and T. Koda, Phys. Status Solidi B 66, 255 (1974).
[9]P. Fiorini, J. C. Merle, and M. Simon (unpublished).
[10]J. B. Grun, C. Comte, R. Levy, and E. Ostertag, in Proceedings of the International Conference on Luminescence, Tokyo, 1976 [J. Lumin. 12/13, 581 (1976)].
[11]D. Fröhlich, E. Mohler, and P. Wiesner, Phys. Rev. Lett. 26, 554 (1971).
[12]R. G. Ulbrich and C. Weisbuch, Phys. Rev. Lett. 38, 865 (1977).
[13]G. Winterling and E. Koteles, Solid State Commun. 23, 95 (1977).
[14]N. Nagasawa, T. Mita, and M. Ueta, J. Phys. Soc. Jpn. 41, 929 (1976).
[15]B. Hönerlage, A. Bivas, and Vu Duy Phach, Phys. Rev. Lett. 41, 49 (1978).
[16]Y. Segawa, Y. Aoyagi, K. Azuma, and S. Namba, Solid State Commun. 28, 853 (1978).
[17]V. M. Agranovich, N. A. Efremov, and H. P. Kaminskaya, Opt. Commun. 3, 387 (1971).
[18]A. Bivas, Vu Duy Phach, B. Hönerlage, U. Rössler, and J. B. Grun, Phys. Rev. B 20, 3442 (1979).
[19]G. Dresselhaus, J. Phys. Chem. Solids 1, 14 (1956).
[20]M. Altarelli and N. O. Lipari, Phys. Rev. B 15, 4898 (1977).
[21]U. Rössler, in *Festkörperprobleme (Advances in Solid State Physics XIX)*, edited by J. Treusch (Pergamon-Vieweg, Braunschweig, 1979), p. 77.
[22]G. L. Bir and G. E. Pikus, *Symmetry and Strain-Induced Effects in Semiconductors* (Wiley, New York, 1974), Secs. 25 and 26.
[23]G. F. Koster, J. O. Dimmock, R. G. Wheeler, and H. Statz, *Properties of the Thirty-two Point Groups* (MIT, Cambridge, Mass., 1963).
[24]G. Fishman, Solid State Commun. 27, 1097 (1978); B. Sermage and G. Fishman, Phys. Rev. Lett. 43, 1043 (1979).
[25]F. Bassani, J. J. Forney, and A. Quattropani, Phys. Status Solidi B 65, 591 (1974).
[26]C. Comte, Opt. Commun. 14, 79 (1975).
[27]E. Hanamura, J. Phys. Soc. Jpn. 39, 1506 (1975).
[28]F. Henneberger and J. Voigt, Phys. Status Solidi B 76, 313 (1976).
[29]T. W. Hänsch, Appl.Opt. 11, 895 (1972).
[30]I. Shoshan, N. N. Danon, and U. P. Oppenheim, J. Appl. Phys. 48, 4495 (1977).
[31]M. G. Littman and H. J. Metcalf, Appl. Opt. 17, 2224 (1978).
[32]Vu Duy Phach and R. Levy, Solid State Commun. 29, 247 (1979).
[33]B. Hönerlage, Vu Duy Phach, and J. B. Grun, Phys. Status Solidi B 88, 545 (1978).
[34]Vu Duy Phach, A. Bivas, B. Hönerlage, and J. B. Grun, Phys. Status Solidi B 86, 159 (1978).
[35]E. Ostertag, thesis, Strasbourg, France (1977) (unpublished).
[36]H. J. Mattausch and Ch. Uihlein, Solid State Commun. 25, 447 (1978) and Phys. Status Solidi B 96, 189 (1979).
[37]M. A. Khan, Phys. Status Solidi B 60, 641 (1973).
[38]B. Hönerlage, C. Klingshirn, and J. B. Grun, Phys. Status Solidi B 78, 599 (1976).